11th International Symposium on Turbulence and Shear Flow Phenomena (TSFP11)
Southampton, UK, July 30 to August 2, 2019

MEASUREMENT OF TURBULENT SQUARE DUCT FLOWS OVER ANISOTROPIC POROUS MEDIA

K. Suga, Y. Okazaki, T. Matsuo, A. Taneo and Y. Kuwata
Department of Mechanical Engineering,
Osaka Prefecture University
Sakai, Osaka 599-8531, Japan
suga@me.osakafu-u.ac.jp

ABSTRACT

To understand the effect of anisotropic permeability on surface turbulence, PIV measurements are performed for square duct flows over two transparent anisotropic porous structures whose ratios of the wall-normal to streamwise permeabilities are 0.8 and 7.8. The obtained results at Re=3500 and 8000 confirm that although turbulence is enhanced by the permeability, turbulence over and under the porous surfaces is insensitive to the wall-normal permeability compared with the other components when the wall-normal permeability is sufficiently large. Near the symmetry planes, Kelvin-Helmholtz type waves are detected at the porous surfaces. While the effects of the wall-normal permeability on the wavelengths are not observed, it is found that their characteristics are similar to those reported in the literature for boundary layer flows over porous media.

INTRODUCTION

For a gas diffusion layer (GDL) of a proton exchange membrane fuel cell (PEMFC), carbon papers whose structures are not isotropic are often used. As the flow Reynolds number of a rectangular channel (duct) flow over a GDL in a PEMFC sometimes reaches to Re$\simeq$3000 (Suga *et al.*, 2014), for designing PEMFCs, it is important to understand surface turbulence over anisotropic porous media in a rectangular duct.

Since we often encounter turbulence over a permeable surface in engineering and environmental flows, many people including the present authors studied turbulent flows over porous media, (e.g. Breugem *et al.*, 2006; Suga *et al.*, 2010, 2017). From those studies, what was confirmed was that the wall permeability affects turbulence near a wall enhancing momentum exchange. Since permeable walls allow flow motions to penetrate into the walls, turbulence is not totally damped resulting in strong wall shear. However, since most of such studies applied isotropic porous media, there are very limited understandings on turbulence over anisotropic porous media. Hence, recently the present authors have performed PIV experiments of turbulent flows over orthotropic porous media (Suga *et al.*, 2018). Here, orthotropic porous media are kinds of anisotropic porous media whose structures are uniform along the coordinate axes. We have suggested that turbulence generation over porous media is insensitive to the wall-normal permeability K_{yy} when $R_{yx} = K_{yy}/K_{xx} \geq 1.0$. Note that the permeability is defined as a second rank tensor as K_{ij} and its diagonal components K_{xx}, K_{yy} and K_{zz} are simply called streamwise, wall-normal and spanwise permeabilities, respectively, in this study.

Table 1. Permeabilities of porous media.

case	φ	K_{xx}	K_{yy}	K_{zz} $(\times 10^{-7}\mathrm{m}^2)$	R_{yx}
case ⊞	0.8	1.9	1.5	1.9	0.8
case □	0.8	1.6	12.5	1.6	7.8

However, it is still unknown what happens when $R_{yx} < 1.0$. In such a case, DNS studies of Abderrahaman-Elena & García-Mayoral (2017); Gómez-de Segura *et al.* (2018) suggested that the turbulence drag might be reduced when $1/R_{yx}$ was extremely large. Rosti *et al.* (2018) also supported this discussion while the drag was increased with $R_{yx} > 1.0$. Those results show us the way to go for devising new drag reducing surfaces while the flows inside porous media of those studies were modelled by the Brinkmann equation (Abderrahaman-Elena & García-Mayoral, 2017; Gómez-de Segura *et al.*, 2018) or were not solved by using idealized surface boundary conditions (Rosti *et al.*, 2018). Hence, the realizability of such drag reducing condition may not be fully convinced. Moreover, the effect of the wall permeability on turbulence under porous surfaces has not been well discussed by experiments due to the difficulty of optical access. Also, the above mentioned understandings are for two-dimensional channel or boundary layer flows, and hence it is unknown whether those understandings are applicable to rectangular duct flows over porous media such as the flows in PEMFCs. Therefore, this study measures both over- and under-surface turbulence of rectangular duct flows at different permeability ratios of $R_{yx} = 0.8$ and 7.8.

EXPERIMENTAL METHOD

Fig.1 illustrates the flow facility and the test section of the present experimental setup. Tracer particles are polymer capsules containing Rhodamine B and their mean diameter and specific gravity are respectively 10 μm and 1.50. Tap water is pumped up from a water tank to a straighter and nozzle section with turbulence grids at the exit, then the flow is fully developed in a 2.0 m long driver duct whose cross section (height$\times$width) is 100×50 mm^2 and enters the test section. The duct consists of solid smooth acrylic walls and a porous layer settled on the bottom wall. The thickness and width of the porous layer are 50 mm which are the same as the height of the clear-fluid-region: $H = 50$ mm. To maintain the optical access to the porous region, transparent acrylic rods with square cross sections are used

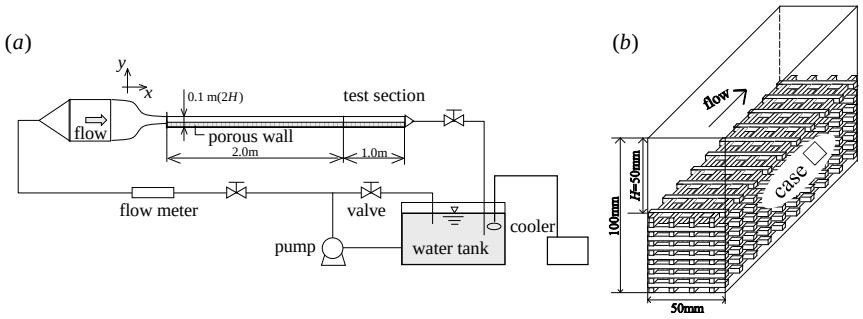

Figure 1. Experimental setup; (*a*) flow facility, (*b*) test section.

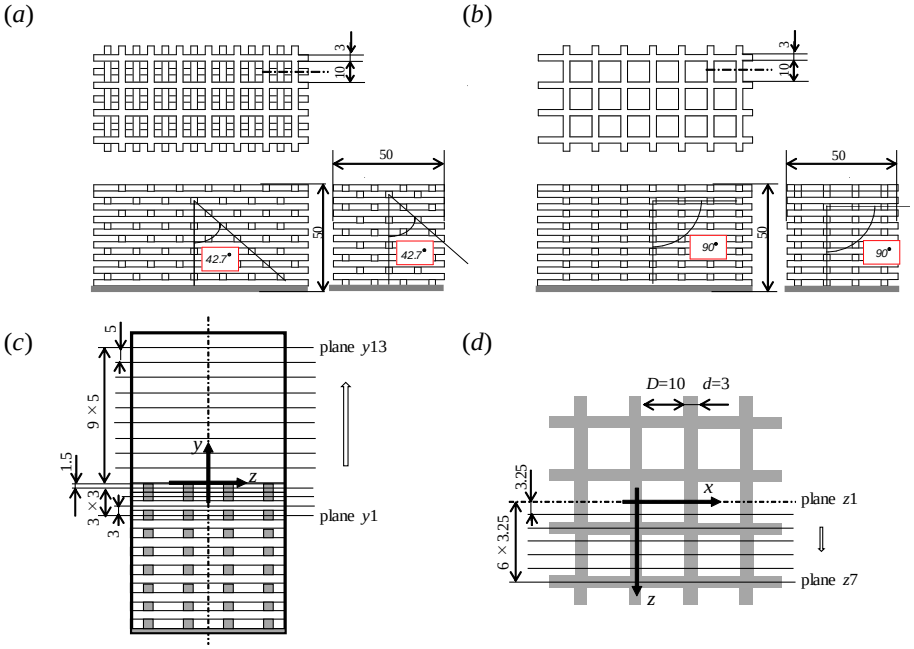

Figure 2. Structures of porous media, measuring sections and definition of the coordinates: (*a*) case ⊞, (*b*) case □, (*c*) measurement planes of $x-z$ plane measurements, (*d*) measurement planes of $x-y$ plane measurements.

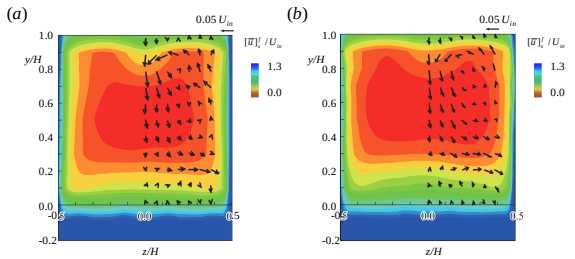

Figure 3. Mean velocity of case □: (*a*) at Re=3500, (*b*) at Re=8000.

to construct two different porous media: cases ⊞ and □, as shown in Fig.2. The sides of square pores and rod sections are $D = 10$ mm and $d = 3$ mm, respectively. The porosity of the porous media is $\varphi = 0.8$ and the measured permeabilities are listed in Table 1. The wall-normal diagonal component of the permeability tensor is designed to be different from the other components by the factors of 0.8 and 7.8 for cases ⊞ and □, respectively. The present planar PIV system consists of a DPSS laser with the wavelength of 532 nm, a high speed CMOS camera, a camera lens with a long-pass filter and a computer for data acquisition. The aspect ratio of the high-speed camera frame is 1.36:1 and the frame resolution is 1632×1200 pixel^2. The laser light sheet is approximately 1.0 mm thickness and illuminates the measuring sections. The streamwise-spanwise (x–z) and streamwise-wall-normal (x–y) plane measurements are performed at Re$= U_{in}H/\nu \simeq 3500$ and 8000. Here, U_{in} is the mean inlet velocity to the square duct. For the x–z plane measurements, as shown in Fig.2(c), 13 planes (plane $y1-y13$) of case □ at $y/H = -0.21, -0.15, -0.09, -0.03, 0.1, 0.2, 0.3, 0.4, 0.5, 0.6, 0.7, 0.8$ and 0.9 are measured. For the x–y plane measurements, as shown in Fig.2(d), 7 planes (plane $z1-z7$) at $z/H = 0.0, 0.065, 0.13, 0.195, 0.26, 0.325$ and 0.39 are measured for both cases ⊞ and □. Note that the porous interface is at $y/H = 0$ and the spanwise symmetry plane is at $z/H = 0$.

To maintain the measuring accuracy inside the porous media, a single measuring section of a x–y plane is divided into three zones: clear flow, interface and porous medium zones. Hence, for each zone, a single recorded frame of the camera covers 75×55, 52×38 or 65×48 mm^2. The number of the particle is adjusted to be about 16 in an interrogation window whose size is set to 32×32 pixel^2. The uncertainty in the measured displacement can be expected to be less than $1/10$ of the diameter of the particle image. Normalizing the uncertainty of this mean displacement of particles yields a relative error of less than 4%.

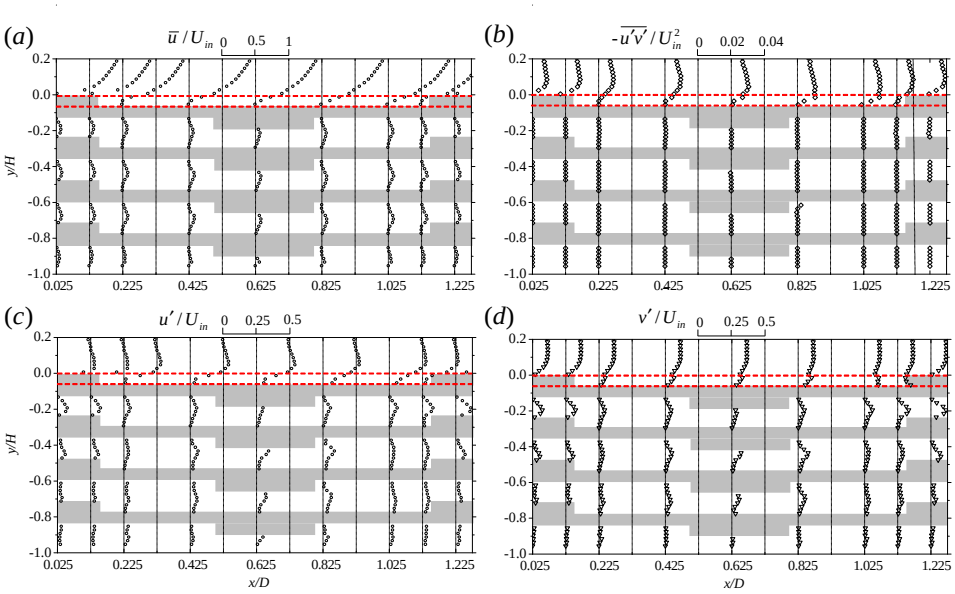

Figure 4. Time averaged turbulence quantities in the symmetry plane (plane $z1$ at $z/H = 0$) in case ⊞ at Re=3500: (a) streamwise velocity, (b) Reynolds shear stress, (c) streamwise turbulent intensity, (d) wall-normal turbulent intensity. Red broken lines show positions at $y = 0$ and $y = -d$.

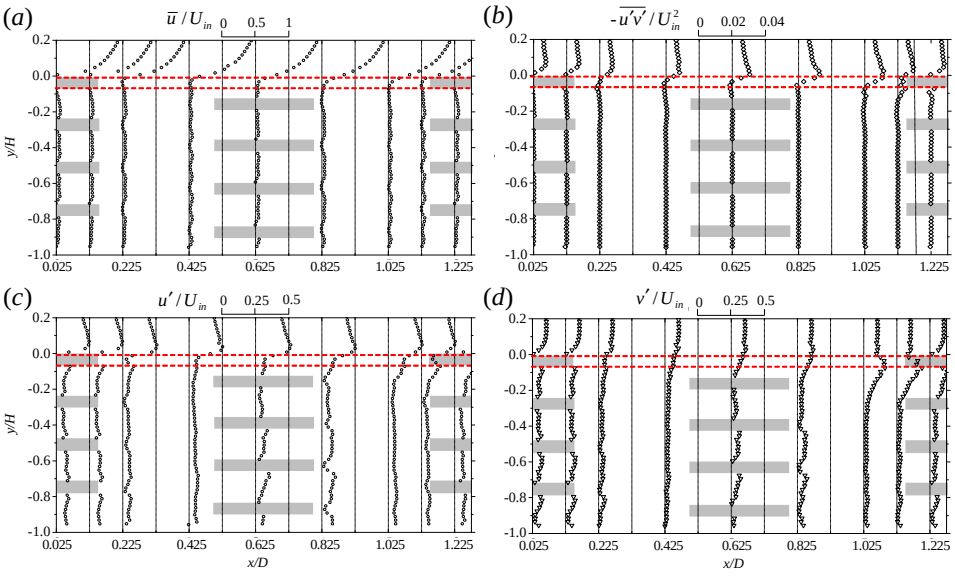

Figure 5. Time averaged turbulence quantities in plane $z4$ at $z/H = 0.195$ in case ⊞ at Re=3500: (a) streamwise velocity, (b) Reynolds shear stress, (c) streamwise turbulent intensity, (d) wall-normal turbulent intensity. Red broken lines show positions at $y = 0$ and $y = -d$.

RESULTS & DISCUSSIONS

Fig.3 shows contour maps of $[\bar{u}]_x^f$ with the cross-sectional velocity vectors of case □ at Re=3500 and 8000. The contour maps are produced with the $x-z$ plane measurement data while the vectors are calculated with the $x-y$ and $x-z$ plane measurement data. Here, overbar denotes time averaging and $[\cdot]_x^f$ denotes fluid-phase averaging in the $x-$direction. It is seen that the cross-sectional secondary flow patterns are very different from the well known patterns of the square duct flow. A large single recirculation is seen near the upper corner and relatively weak recirculation can be seen near the interface. These flow patterns verify the numerical simulation of Samanta *et al.* (2015) using the volume averaged N-S equation for the porous region. Due to the cross-sectional secondary flows, $[\bar{u}]_x^f$ shows skewed distribution near the top wall at $y/H = 1.0$. However, its distribution becomes much flatter near the porous interface at $y/H = 0.0$ and it is considered that the flow characteristics around the porous interface may be regarded as quasi two-dimensional near the symmetry plane.

To see the flow characteristics inside the porous region, Figs.4-7 show time averaged streamwise velocity:

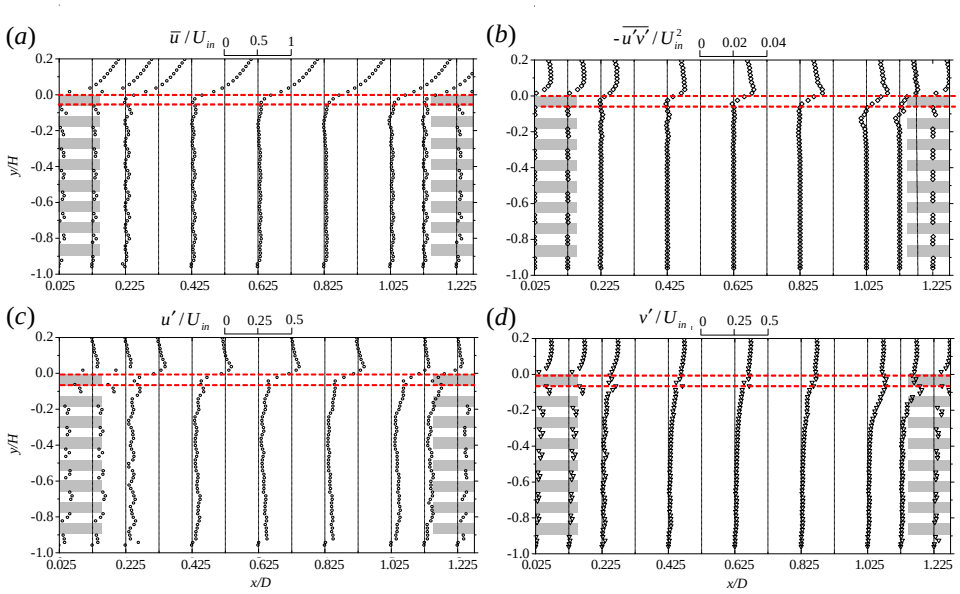

Figure 6. Time averaged turbulence quantities in the symmetry plane (plane $z1$ at $z/H = 0$) in case □ at Re=3500: (a) streamwise velocity, (b) Reynolds shear stress, (c) streamwise turbulent intensity, (d) wall-normal turbulent intensity. Red broken lines show positions at $y = 0$ and $y = -d$.

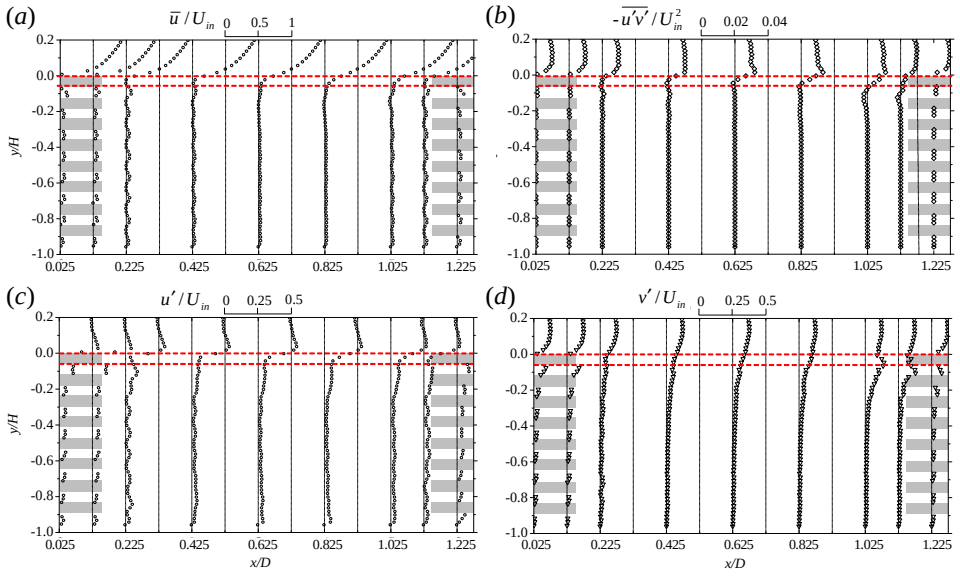

Figure 7. Time averaged turbulence quantities in plane $z4$ at $z/H = 0.195$ in case □ at Re=3500: (a) streamwise velocity, (b) Reynolds shear stress, (c) streamwise turbulent intensity, (d) wall-normal turbulent intensity. Red broken lines show positions at $y = 0$ and $y = -d$.

$\bar{u}$, Reynolds Shear stress: $-\overline{u'v'}$, and turbulent intensities: u', v' at Re=3500. Figs.4 and 5 are for the symmetry plane: plane $z1$ at $z/H = 0$, and plane $z4$ at $z/H = 0.195$, in case ⊞ while Figs.6 and 7 are those in case □. The position of $x/D = 0$ corresponds to the symmetry plane of the transverse rods as shown in Fig.2 (d). Depending on the porous structure, the streamwise mean velocity distribution profile changes obviously. Indeed, in case ⊞ shown in Figs.4 (a) and 5 (a), the solid structures are very different and the corresponding mean velocity profiles are also different while in case □ as shown in Figs.6 (a) and 7 (a), since the solid structures are the same the mean velocity profiles look very similar. However, when we focus on the penetration depth, which is defined as the length needed for the quantity to vanish under the interface, it is always less than the first rod height. Accordingly, the Reynolds shear stress is also vanish generally up to $y = -d$. As for the turbulent intensities, Figs.4-7 indicate that the penetration lengths are much longer suggesting that turbulent eddies go into the media more deeply than the mean flow motions.

As discussed with Fig.3, the flows are reasonably two-dimensional over the interface near the symmetry plane.

Hence, to see the general flow statics, x–z plane averaging is applied by the trapezoidal rule using the x–y plane data of planes $z1-z4$ at $z/H=0.0$, 0.065, 0.31 and 0.195. By this procedure, the x–z plane covers 4 $\times$1 unit-cells of the porous structure. Figs.8 and 9 compare the plane averaged streamwise mean velocity, Reynolds stress and turbulent intensities at Re=3500 and 8000, respectively. For the profiles in the clear flow region, although there are slight discrepancies between the cases ⊞ and □, two cases show nearly the same profiles. This trend supports our previous conclusion in Suga *et al.* (2018) which suggested that although turbulence generation over porous media was enhanced by the permeable surface, it is rather insensitive to the wall-normal permeability K_{yy} compared with K_{xx}. Indeed, although K_{yy} of case □ is 8.3 times larger than that of case ⊞, the discrepancy between the two cases cannot be considered to reflect such a large ratio.

Instead of the insensitivity to K_{yy}, Suga *et al.* (2018) showed that a 25 % increase of K_{xx} produced a certain amount of turbulence enhancement. However, in this study, case ⊞ whose K_{xx} is 19 % larger than that of case □ does not show meaningful difference in the Reynolds shear stress and turbulent intensity profiles over the porous layer at both Re=3500 and 8000. When we consider that the permeability induces penetrating vortex motions into the porous surface, the smaller one among K_{xx}, K_{yy} and K_{zz} is considered to affect more the fluid motions. In fact, for case ⊞ the smallest permeability component is $K_{yy}=1.5\times10^{-7}\mathrm{m}^2$ while for case □ it is $K_{xx}=1.6\times10^{-7}\mathrm{m}^2$. Since they are nearly the same, the discrepancies in the flow characteristics may not be produced. With regard to this, the conditions of the DNS studies of Abderrahaman-Elena & García-Mayoral (2017); Gómez-de Segura *et al.* (2018); Rosti *et al.* (2018) were very different from those of the present experiments since the scales of their wall-normal permeabilities were much smaller than the size of the smallest turbulent eddies.

From the velocity profiles under the surface, there is no visible difference in the penetration depths in Figs.8(a) and 9(a) though the difference in K_{yy} of two cases is large. It is clear that the penetration depths of the mean velocity of case ⊞ is less than $y/H=0.06$ which is the height d of the square rod constructing the porous media. Even though K_{yy} becomes 8.3 times larger in case □, the penetration depth does not increase at all. Correspondingly, as seen in Figs.8(b) and 9(b), the Reynolds stresses of both cases damp quickly until $y/H=0.06$ and it is confirmed that there seems no turbulence generation below there. As for the turbulent intensities shown in Figs.8(c,d) and 9(c,d), as discussed with Figs.4-7, both components show longer penetration depths than those of the mean velocity and Reynolds shear stress profiles. Among them, the wall-normal fluctuations shown in Figs.8(d) and 9(d) show longer distances to be damped in the porous media than the mean velocity. These suggest that although there is no shear generation, turbulent vortices penetrate and dissipate at a deeper position inside the porous media. Particularly for the wall-normal direction, it is supposed that flow fluctuations are induced by the pressure fluctuations over the surface which propagate more deeply inside the porous media. These trends confirm the results reported by Breugem *et al.* (2006) who applied the volume averaged N-S equation for the porous medium region. It is considered that obvious fluctuations inside porous media come from the porous structures. Although the penetrations of the turbulent intensities are similar, the levels of the intensities of case ⊞ in the porous layer are slightly

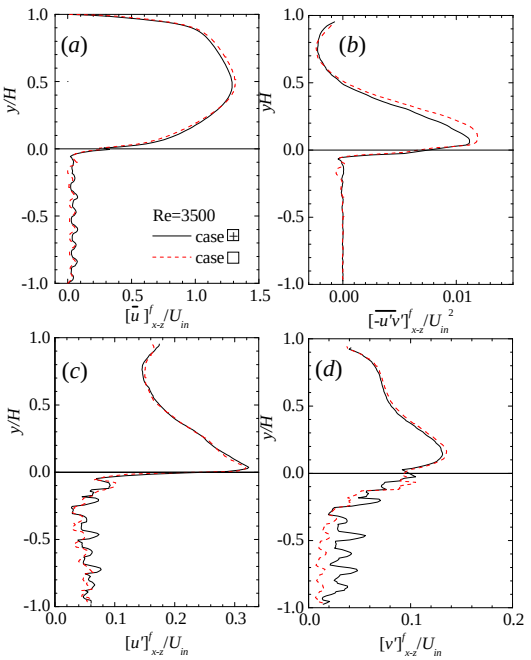

Figure 8. Comparison of plane averaged turbulence quantities at Re=3500: (a) streamwise velocity, (b) Reynolds shear stress, (c) streamwise turbulent intensity, (d) wall-normal turbulent intensity.

larger than those of case □. This trend corresponds to the magnitude of the streamwise permeability K_{xx}.

Fig.10 shows one-dimensional spectrum of streamwise velocity fluctuations $E_{11,x}$ at $y/H=0.2, 0.0$ and -0.02. Those locations correspond to over, on and under the surface, respectively. Both cases ⊞ and □ on the surfaces ($y/H=0$) show clear peaks. At Re=3500 shown in Fig.10(a,b), the peaks of $y/H=0.0$ locate at $f=0.25$ Hz that corresponds to the wavelength of $\lambda_w=[\overline{u}_w]^f_{x-z}/f$=0.082 m due to the slippage velocity of $[\overline{u}_w]^f_{x-z}=0.3U_{in}$ as shown in Fig.8(a). At Re=8000 of case ⊞, the peak of $y/H=0.0$ locates at $f=0.5$ Hz that corresponds to the wavelength of λ_w=0.11m while for case □, it locates at $f=0.6$ Hz that corresponds to the wavelength of λ_w=0.09 m since the slippage velocity increases to $0.35U_{in}$. Accordingly clear effects of the wall-normal permeability on the wavelengths are not observed. Although the locations of the peaks of $y/H=0.2$ and -0.02 sometimes slightly shift from those of $y/H=0.0$, the corresponding frequencies are very similar to those of $y/H=0.0$. This is because energy of the waves generated at the surfaces propagates to both over- and under-surface regions.

In the fully developed mixing layers, the normalized wavelength of the Kelvin-Helmholtz type coherent eddies by the vorticity thickness $C_\lambda=(\lambda_x/\delta_\omega)$ is known to be $3.5\le C_\lambda\le5$. For flows over the porous walls, the DNSs by Breugem *et al.* (2006); Kuwata & Suga (2017) and the experiments by Suga *et al.* (2018) indicated $3.4\le C_\lambda\le5.5$ when the the boundary-layer thickness δ_p is considered to be equivalent to the vorticity thickness δ_ω. Since the mean velocity has a peak at $y/H\simeq0.5$ as shown in Figs.8(a) and 9(a), δ_p is assumed to be $\delta_p\simeq0.5H$ in this study. In such a condition, the wavelength λ_w of cases ⊞ and □ at Re=3500 produces $C_\lambda=\lambda_w/\delta_p=3.3$. For cases ⊞ and □ at Re=8000, $C_\lambda=4.4$ and 3.6, respectively. These values

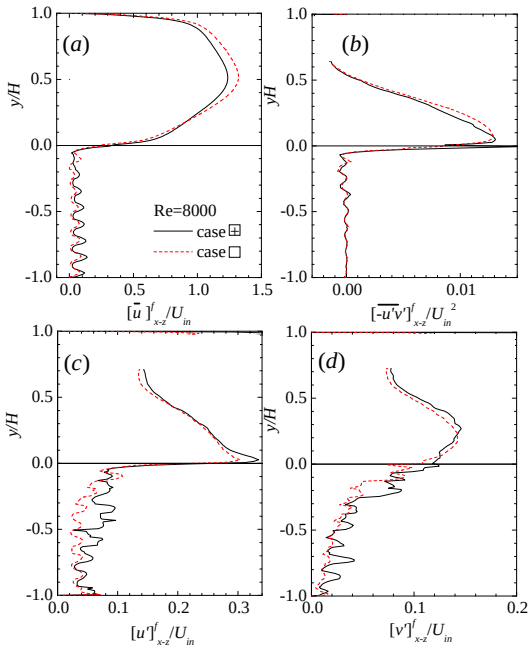

Figure 9. Comparison of plane averaged turbulence quantities at Re=8000: (*a*) streamwise velocity, (*b*) Reynolds shear stress, (*c*) streamwise turbulent intensity, (*d*) wall-normal turbulent intensity.

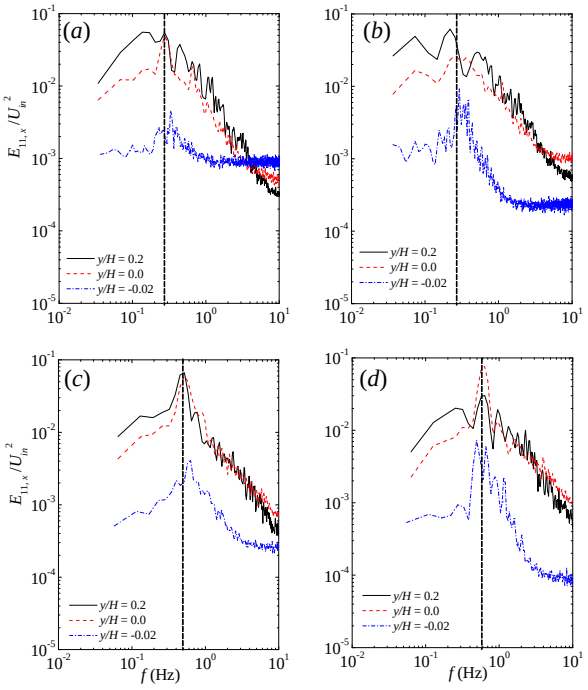

Figure 10. One-dimensional streamwise spectrum of u': (*a*) case ⊞ at Re=3500, (*b*) case □ at Re=3500, (*c*) case ⊞ at Re=8000, (*d*) case □ at Re=8000. Black thin broken lines correspond to the frequencies of peak locations at the surface: $y/H = 0.0$.

generally accord with the range reported by the previous studies of turbulence over porous media. Therefore, even in square duct flows it is suggested that transverse waves generated by Kelvin-Helmholtz type instability are formed at the porous surfaces.

CONCLUSIONS

PIV measurements have been performed for turbulent square duct flows over two transparent anisotropic porous media whose ratios of the wall-normal to streamwise permeabilities are 0.8 and 7.8 at Re=3500 and 8000. It is confirmed that although turbulence is enhanced by the permeability, turbulence over and under the porous surfaces is rather insensitive to the wall-normal permeability compared with the other components when the wall-normal permeability is sufficiently large. It is also confirmed that the turbulent intensities penetrate more deeply than the mean velocity and the wall-normal fluctuation needs a longer distance to be damped in the porous media than the streamwise component. This suggests that although there is no shear generation, turbulent vortices penetrate and dissipate at deeper locations inside porous media. It is considered that turbulent fluctuations are drawn into the porous media by the pressure fluctuations over the surface which propagate more deeply inside the porous media. Near the symmetry planes, Kelvin-Helmholtz type waves are detected at the porous surfaces. While the effects of the wall-normal permeability on the wavelengths are not observed, it is found that their characteristics are similar to those reported in the literature for boundary layer flows over porous media.

REFERENCES

Abderrahaman-Elena, Nabil & García-Mayoral, Ricardo 2017 Analysis of anisotropically permeable surfaces for turbulent drag reduction. *Phys. Rev. Fluids* **2**, 114609.

Breugem, W. P., Boersma, B. J. & Uittenbogaard, R. E. 2006 The influence of wall permeability on turbulent channel flow. *J. Fluid Mech.* **562**, 35–72.

Kuwata, Y. & Suga, K. 2017 Direct numerical simulation of turbulence over anisotropic porous media. *J. Fluid Mech.* **831**, 41–71.

Rosti, M. E., Brandt, L. & Pinelli, A. 2018 Turbulent channel flow over an anisotropic porous wall – drag increase and reduction. *J. Fluid Mech.* **842**, 381–394.

Samanta, A., Vinuesa, R., Lashgari, I., Schlatter, P. & Brandt, L. 2015 Enhanced secondary motion of the turbulent flow through a porous square duct. *J. Fluid Mech.* **784**, 681–693.

Gómez-de Segura, G., Sharma, A. & García-Mayoral, R. 2018 Turbulent drag reduction using anisotropic permeable substrates. *Flow, Turb. Combust.* **100**, 995–1014.

Suga, K., Matsumura, Y., Ashitaka, Y., Tominaga, S. & Kaneda, M. 2010 Effects of wall permeability on turbulence. *Int. J. Heat Fluid Flow* **31**, 974–984.

Suga, K., Nakagawa, Y. & Kaneda, M. 2017 Spanwise turbulence structure over permeable walls. *J. Fluid Mech.* **822**, 186–201.

Suga, K., Nishimura, W., Yamamoto, T. & Kaneda, M. 2014 Measurements of serpentine channel flow characteristics for a proton exchange membrane fuel cell. *Int. J. Hydrogen Energy* **39**, 5942–5954.

Suga, K., Okazaki, Y., Ho, U. & Kuwata, Y. 2018 Anisotropic wall permeability effects on turbulent channel flows. *J. Fluid Mech.* **855**, 983–1016.